

# Carbon Segregation in CoCrFeMnNi High-Entropy Alloy Driven by High-Pressure Torsion at Room and Cryogenic Temperatures

Yemao Lu,\* Horst Hahn, and Yulia Ivanisenko

Herein, a CoCrFeMnNi high-entropy alloy with reduced Cr content and with the addition of 2 at% C interstitial is processed via high-pressure torsion (HPT) under 6.5 GPa by three turns at room and cryogenic temperatures. The microstructure is investigated by transmission electron microscopy (TEM) and atom probe tomography (APT). The results indicate that C atoms segregate at the boundaries of the nanograins in the sample processed at room temperature, while the sample processed at cryogenic temperature does not show any notable segregations of carbon.

## 1. Introduction

CoCrFeMnNi high-entropy alloys (HEAs) with face-centered cubic (FCC) structure have recently garnered extensive interests due to numerous improved and unique properties in respect to conventional alloys,<sup>[1–3]</sup> especially the remarkable mechanical properties at cryogenic temperatures.<sup>[4,5]</sup> Nevertheless, FCC HEAs usually show notable ductility but insufficient strength. Alloying with interstitial elements is one of possible approaches to increase the strength and maintain reasonable ductility.<sup>[6–8]</sup> In addition, severe plastic deformation (SPD) techniques, for instance, high-pressure torsion (HPT), can be used to obtain ultrafine grained metallic alloys with extremely high strength.<sup>[9,10]</sup> Carbon interstitial not only contributes to improve solid solution strengthening and lattice friction stress but also significantly enhances the grain refinement ability due to the

strong effect on dislocation cross-slip.<sup>[7,11]</sup> Meanwhile, carbon can easily segregate on the defects during SPD processing at room and elevated temperatures,<sup>[12–14]</sup> which provides extra strengthening contribution. Recently, nanocrystalline CoCrFeNiMn alloy with a mean grain size of  $\approx 50$  nm was obtained by HPT at room temperature (300 K), which is presented in a single FCC phase.<sup>[15–17]</sup> It suggested a significant increase of the strength with a sacrifice of ductility. Later, some works performed cryo-HPT processing at liquid

nitrogen temperature (77 K) to explore the nanocrystalline structures and mechanical properties at such cryogenic temperature.<sup>[18,19]</sup> It was reported that a martensitic phase transformation from FCC to hexagonal close-packed HCP structure during the deformation occurs, while the hardness values of the sample processed by HPT at 77 K are much less mainly due to lower dislocation density.<sup>[19]</sup> However, only few works were conducted with interstitial alloyed CoCrFeMnNi system FCC structured HEAs to approach ultrafine-grained or nanocrystalline structures using plastic deformation methods at cryogenic temperatures,<sup>[7,20]</sup> especially with HPT method. Additionally, the carbon interstitial effect on the grain refinement behavior has not been systematically studied at cryogenic temperature in FCC structured HEAs. In the present work, we aimed to understand how HPT straining can drive carbon interstitial to diffuse at cryogenic and room temperature.

## 2. Results and Discussion

Figure 1 displays the X-ray diffraction patterns of Co<sub>1</sub>Cr<sub>0.25</sub>Fe<sub>1</sub>Mn<sub>1</sub>Ni<sub>1</sub>-2% C alloy deformed at 300 and 77 K. After HPT, only single FCC structure is present in both specimens, in contrast to a recent work,<sup>[18]</sup> where a formation of about 30% of HCP phase was revealed after HPT processing at 77 K in the equiatomic CoCrFeMnNi HEA. Most likely this difference arises from higher pressure of 7.8 GPa applied at HPT in the work.<sup>[18]</sup> Note that the HCP phase has not been found in CoCrFeMnNi HEA processed by HPT at 6 GPa at 77 K in ref. [19], which is similar to the HPT conditions in our case. No evident shift of respective X-ray diffraction (XRD) peak positions is observed between XRD patterns (inset in Figure 1) which points toward the same lattice parameter of FCC phase in samples processed at both temperatures. The broadening of XRD peaks demonstrates that numerous lattice defects developed in

Y. Lu, H. Hahn, Y. Ivanisenko  
Institute of Nanotechnology  
Karlsruhe Institute of Technology  
Hermann-von-Helmholtz-Platz 1, 76344 Eggenstein-Leopoldshafen,  
Germany  
E-mail: yemao.lu@partner.kit.edu

Y. Lu  
Karlsruhe Nano-Micro Facility  
Karlsruhe Institute of Technology  
Hermann-von-Helmholtz-Platz 1, 76344 Eggenstein-Leopoldshafen,  
Germany

The ORCID identification number(s) for the author(s) of this article can be found under <https://doi.org/10.1002/adem.202201473>.

© 2020 The Authors. Advanced Engineering Materials published by Wiley-VCH GmbH. This is an open access article under the terms of the Creative Commons Attribution-NonCommercial License, which permits use, distribution and reproduction in any medium, provided the original work is properly cited and is not used for commercial purposes.

DOI: 10.1002/adem.202201473

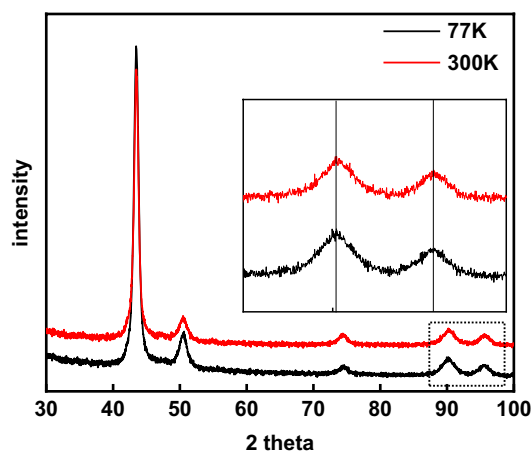
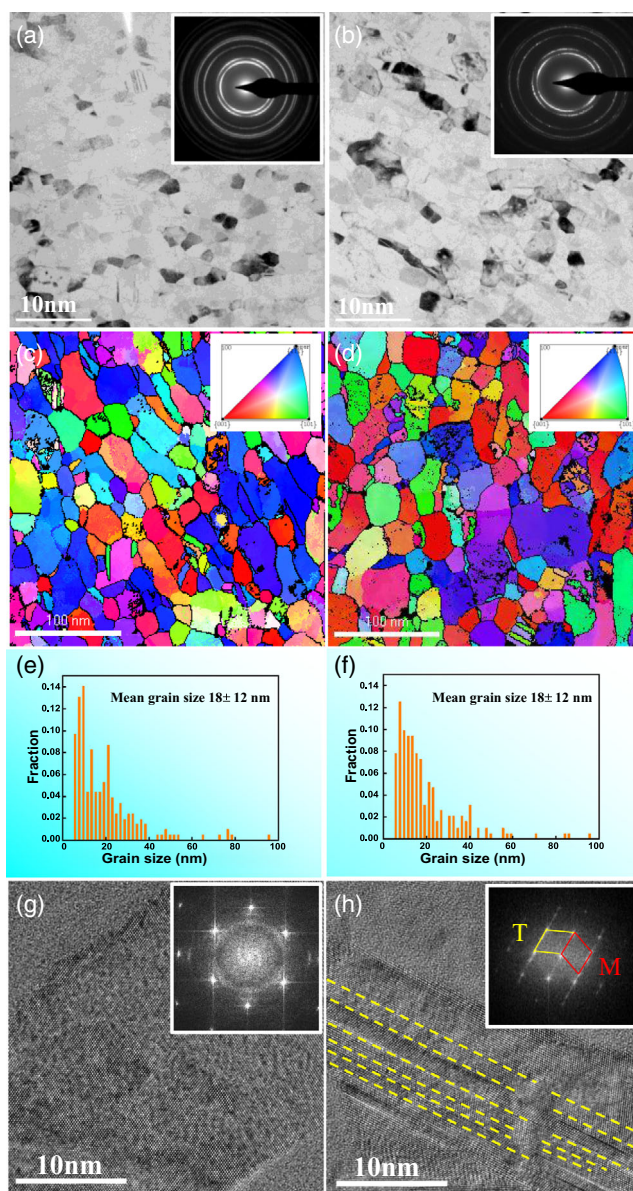


**Figure 1.** XRD patterns of the alloys processed by HPT at room temperature (300 K) and at cryogenic temperature (77 K). Inset is the zoomed high-angle range of the spectrum; no XRD peak shift between the 300 and 77 K samples is detected.

the FCC matrix during HPT processing, indicating a high density of defects, such as high-angle grain boundaries (GBs) and dislocations.

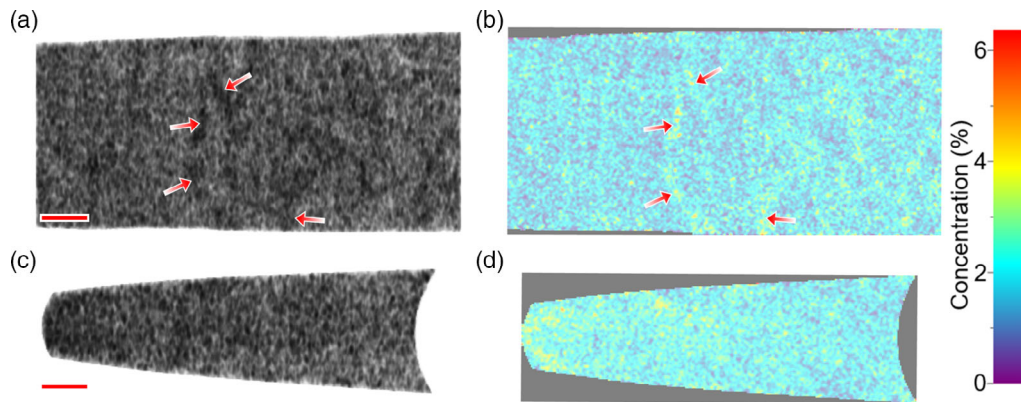
The microstructures of the 300 and 77 K samples corresponding to the sample region with saturated microhardness are shown in **Figure 2**. The bright-field images in **Figure 2a,b** illustrate the nanoscaled uniform microstructure. The corresponding selected area electron diffraction (SAED) patterns indicate that both samples exhibit single FCC phase, suggesting that no precipitation or phase transformation occurred during and after HPT processing. Automated crystal orientation mapping (ACOM) maps are shown in **Figure 2c,d**. Nanoscale grains are separated by high-angle GBs ( $>15^\circ$ ) shown with black lines. In addition, several nanotwins can be found in orientation maps in both alloys. However, due to the limitation of scanning resolution in the microprobe condition, nanotwins with a width less than 4 nm could not be detected especially in 77 K alloy. The grain size distribution histograms for the two HPT conditions are shown in **Figure 2e,f**, which indicate that the average grain size of the two samples is approximately around  $\approx 18 (\pm 12)$  nm. Typical high-resolution transmission electron microscopy (TEM) images of these two samples are shown in **Figure 2g,h**, respectively. The inserted fast Fourier transforms (FFTs) show the  $^{111}$  zone axis in both samples. Apparently, the amount of deformation twins was relatively low in the 300 K sample. However, there are plentiful nanotwins with a thickness between 1 and 4 nm in the 77 K one as shown in **Figure 2h**, marked by yellow dashed lines, and the related FFT provides significant evidence of  $\Sigma 3$  boundaries in (011) plane of FCC phase. In fact, nanotwins were observed in almost all the grains with the  $^{111}$  zone axis normal to the sample surface (i.e., in all grains suitably oriented for observation of twins in HRTEM) in 77 K sample.

The chemical composition and the elemental distribution in studied alloy were analyzed using atom probe tomography (APT) method, as shown in **Figure 3** and S1, Supporting Information. As the grain size of both alloys is around  $\approx 18$  nm, the cuboids of 20 nm thickness were sliced from the original APT volumes to



**Figure 2.** TEM characterization of  $\text{Co}_1\text{Cr}_{0.25}\text{Fe}_1\text{Mn}_1\text{Ni}_1$  alloy with addition of 2 at% C HPT-deformed at a,c,e,f) 300 K and b,d,f,h) 77 K. (a) and (b) show the bright-field TEM images with inserted selected area diffraction patterns; (c) and (d) are orientation maps evaluated from ACOM and corresponding color coding; (e) and (f) are the grain size distribution histograms; (g) and (h) show the HRTEM images and corresponding fast Fourier transform. The TEM samples were extracted from HPT disc in the hardness saturation area at a distance of 6 mm from the center.

avoid crystal overlapping. The carbon volume rendering map in **Figure 3a** shows that the carbon atoms are not homogeneously distributed in this sample but have segregated along the surfaces, which are most probably GBs indicated by red arrows. However, this significant segregation phenomenon was not pronounced in the 77 K sample, as shown in **Figure 3c**. Additionally, the 2D contour color maps of C concentration are illustrated in **Figure 3b** for 300 K sample and in **Figure 3d** for 77 K sample. The periodic variation of carbon concentration is clearly observed in



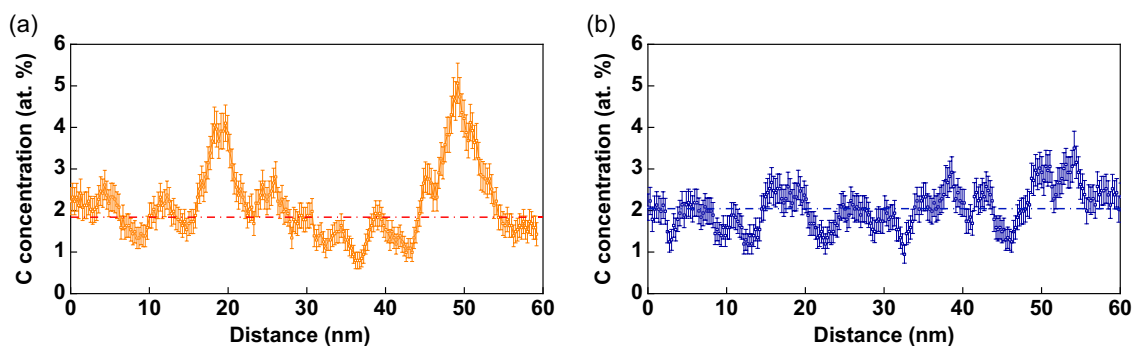
**Figure 3.** Selected APT reconstructions with a thickness of 20 nm. C volume rendering of samples processed at a) 300 K and c) 77 K samples. Corresponding 2D contour color maps of C concentration in (b) and (d), respectively. The arrows in (a) indicate the sites of carbon segregation. The scale bar is 20 nm in all images.

Figure 3b upon those narrow areas with higher C concentration up to 4 at% are situated at a distance comparable with the mean grain size, which indicated a C segregation on the GBs marked by red arrows. Yet, for the 77 K sample in Figure 3d, the areas with high C concentration are mainly located at the APT sample tip region, which may relate to the contaminations induced by sample preparation in the focused ion beam (FIB) system. Let us emphasize that the APT sample (a needle with base radius of 50 nm and a length of 150 nm) contains approximately 100 grains with several hundreds of GBs. Therefore, the obtained results are statistically valid. Meanwhile, the metallic constituents were distributed homogeneously as shown in Figure S1, Supporting Information. Therefore, it seems that carbon atoms segregate to crystalline defects like GBs, which more likely present with a high density in severe deformed alloys.<sup>[14]</sup> The difference between the segregation behavior at 300 and at 77 K hints that the C atom diffusion during the deformation process is insufficient at the low temperature.

In order to quantitatively analyze the fluctuations of carbon concentration in the matrix, 1D concentration profiles were plotted for a cuboid shaped slab with dimensions  $5 \times 5 \times 60 \text{ nm}^3$  along the Z-direction. Two typical linear concentration profiles of carbon for both alloys are shown in **Figure 4**. The inserted horizontal dashed lines correspond to the average C concentration of the selected APT volume. In the present study, the

nominal carbon content in the alloy is 2 at%, which is rather low concentration and usually leads to a large deviation in the statistics. As shown in Figure 4a, the mean C concentration is around 1.84 at%; however, two peaks with a concentration of  $\approx 4\text{--}5 \text{ at}\%$  reveal the pronounced C segregation in the 300 K sample. However, the fluctuations of C concentration were plotted in Figure 4b without any noticeable peak implying that the C segregations were not formed during the HPT process at 77 K in the studied alloy, despite a relatively higher mean C content of 2.04 at%.

Normally, carbon atoms can easily segregate to the lattice defects like dislocations, subgrain and GBs in both body-centered cubic (BCC) and FCC alloys.<sup>[13,14,21]</sup> In order to understand why notable carbon segregations were not observed in the sample processed at 77 K, we should consider two points: 1) the source of carbon atoms to form segregations, and 2) the transport mechanisms for carbon atoms to the segregation sites. In our previous article,<sup>[11]</sup> we have shown that as-melted  $\text{Co}_1\text{Cr}_{0.25}\text{Fe}_1\text{Mn}_1\text{Ni}_1$  alloy with the addition of 2 at% C contains carbides precipitated along GBs. We argued that the dissolution of these carbides during HPT released carbon atoms that subsequently segregated to GBs. This phenomenon was also found in C45 steel processed by HPT at room temperature.<sup>[14]</sup> Present investigation indicates that HPT process at 77 K most likely does not lead to a dissolution of carbides, but rather to their refinement. This directly follows



**Figure 4.** Linear concentration profiles of C atoms evaluated from the APT measurements of the samples processed by HPT at a) 300 K and b) 77 K.

from the fact that the carbon concentration in the FCC matrix is the same in samples after HPT processing at both temperatures, as shown by the XRD determination of lattice parameter (Figure 1). Indeed, released carbon atoms as a result of carbides dissolution can either dissolve in the lattice thus leading to its expansion, or form segregations. As none of that is observed in the sample processed by HPT at 77 K, we conclude that at that temperature carbides are more stable against mechanically driven decomposition. As an example, the refined carbide particle was found at grains triple junction position in the 77 K sample (see Figure S2, Supporting Information). The reasons for the enhanced stability of carbides at 77 K are not fully understood yet and require further investigations with the help of thermodynamic calculations, which is over the scope of present work. Here, we can suggest that it might be somehow related to frozen atom transport mechanisms such as dislocation drag,<sup>[22]</sup> dislocation pipe diffusion,<sup>[23]</sup> nonequilibrium GB diffusion,<sup>[24]</sup> and even vacancy-assisted diffusion,<sup>[25]</sup> due to high energy barrier at cryogenic condition according to Fick's law.<sup>[26]</sup>

Another interesting observation of the present research is the formation of numerous twins inside of the nanocrystalline grains in 77 K sample (Figure 2f). CoCrFeMnNi-type fcc HEAs are known to exhibit excellent mechanical properties at cryogenic temperatures, which is caused by the activation of twinning deformation.<sup>[5,7,27]</sup> In the abovementioned works, a transition to twinning deformation is related to the pronounced temperature dependence of the yield strength. High flow stress at cryogenic temperature is an important trigger for the development of deformation twins in FCC HEAs.<sup>[28–30]</sup> Additionally, the activation of deformation twinning can be related to the temperature dependence of the stacking fault energy (SFE) as shown by first-principle quantum mechanical methods.<sup>[31]</sup>

Finally, let us regard the hardness variation from the center to the edge of the HPT samples, which is shown in Figure 5. The hardness of both samples significantly increased from the HPT disc center to the area with saturated value of  $\approx 630$  HV. As the hardness measurements were carried out immediately after the HPT processing at 77 K, we assume that the effect of the

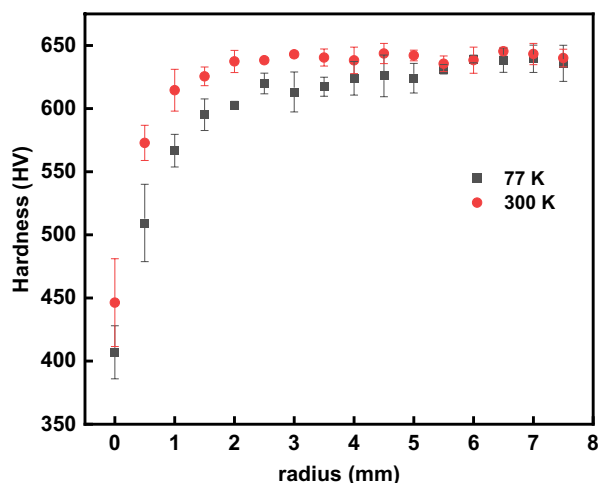


**Figure 5.** The variation of hardness along the HPT disk radius of samples processed by HPT at room temperature (300 K) and at cryogenic temperature (77 K).

microstructure recovery at room temperature on the hardness values is negligible. Hence, the hardness exhibits a saturation at a radius of about 2.5 mm, which corresponds to an equivalent strain of  $\approx 33$ , indicating that the grain size and defects density are at the same level in both samples. Let us note that in recent works on nanocrystalline CoCrFeMnNi alloy processed by HPT at 77 and at 300 K, microhardness values were about 10% lower in the 77 K sample than these in the sample prepared at 300 K.<sup>[18,19]</sup> Something similar is observed in the present work for sample areas corresponding to equivalent strains at HPT lower than 60 (Figure 5). In refs. [18,19], the main reason for lower hardness in samples processed at 77 K was attributed to a reduced dislocation density in the FCC phase.

Taking into account close values of hardness for both samples shown in Figure 5, we assume the yield strengths of 300 and 77 K samples could be comparable. In our previous study, we confirmed that 300 K alloy demonstrated remarkably high yield strength of  $\approx 2.4$  GPa, but zero ductility, which we attributed to carbon segregations on GBs.<sup>[11]</sup> We argued that as GB sliding is a main deformation mechanism in such nanostructured alloys, and GBs are decorated with C segregations, GB sliding is retarded in 300 K alloy, leading to brittle behavior in tensile test. One can expect that reduced carbon segregation to GBs in 77 K alloy may lead to a reasonable ductility in 77 K sample.

### 3. Conclusion

In the present study, Co<sub>1</sub>Cr<sub>0.25</sub>Fe<sub>1</sub>Mn<sub>1</sub>Ni<sub>1</sub> alloy with 2 at% Carbon has been deformed using HPT at room and liquid nitrogen temperatures and carbon segregation behavior has been studied. Investigations allowed to conclude that the nanostructured single-phase FCC HEA processed at room temperature shows carbon segregations at GBs or in areas with high density of dislocations. However, cryogenic deformation is unfavorable to carbon segregation formation mainly due to enhanced stability of carbides against mechanically driven dissolution and high diffusion energy barrier at low temperature. Finally, the hardness values of samples processed at room and cryogenic temperatures are similar and very high at 630 HV in the saturation mainly due to the similar grain size distributions and defect densities.

### 4. Experimental Section

Co<sub>1</sub>Cr<sub>0.25</sub>Fe<sub>1</sub>Mn<sub>1</sub>Ni<sub>1</sub> (subscripts indicate the molar fraction of the respective component) alloy was prepared by vacuum induction melting using high purity elements (99.9 wt%) with the addition of 2 at% C. In the following, the studied alloy is named as Co<sub>1</sub>Cr<sub>0.25</sub>Fe<sub>1</sub>Mn<sub>1</sub>Ni<sub>1</sub>-2% C for brevity. The amount of Cr in alloys was reduced in order to avoid the formation of massive chromium carbides and to increase the solubility of carbon in the FCC lattice.<sup>[7]</sup> Despite of it, the as-melted alloy contained lamellar carbides precipitated along GBs.<sup>[7,11]</sup> For the HPT processing, the as-melted ingot was sectioned to obtain discs with a diameter of 15 mm and an initial thickness of 0.8 mm. HPT process was performed at room temperature (300 K) and at liquid nitrogen temperature (77 K) under a hydrostatic pressure of 6.5 GPa for three turns with a rotation speed of 0.5 rpm. The processing at 77 K was performed as follows. The sample was fixed between the HPT anvils; after that the anvils were immersed into a liquid nitrogen bath, 30 min were left for temperature stabilization, and a continuous supply of liquid nitrogen was provided during deformation. Hardness measurements were carried out immediately

after the processing by HPT at 77 K. Vickers microhardness was measured with a load of 500 g with a dwell time of 10 s on the polished surface of the samples using a Buehler Micromet-5104 device. The distance between indents was maintained at a constant value of 0.5 mm. XRD measurements were performed using a Philips X'Pert powder diffractometer with a Cu K $\alpha$  anode. The conventional and high-resolution TEM measurements were carried out using ThermoFisher Themis-Z at 300 kV with double aberration corrector. ACOM-TEM was collected by FEI Tecnai F20-ST at 200 kV in  $\mu$ p-STEM mode equipped with the NanoMegas ASTAR system using a pixel size of 1 nm. Crystallites with an area under 20 pixels (corresponding to an equivalent diameter  $\approx$ 5 nm) were not included into the statistics due to their overlapping along the electron beam path. APT measurements were conducted using Cameca-LEAP 4000 $\times$  HR instrument in voltage probe mode at 55 K, a pulse rate of 200 kHz, and a target detection rate of 0.3%. The reconstruction of APT data was performed with AP-Suite6 software. TEM lamellae and APT tips for microstructure characterization were extracted from HPT disc at distance of 6 mm from the center and prepared using a FEI Strata 400 equipped with Ga FIB. For the sample produced at 77 K, the tips for APT measurements were prepared by FIB just after the hardness measurements were finished; subsequently, the tips were stored in the LEAP 4000 $\times$  HR chamber.

## Supporting Information

Supporting Information is available from the Wiley Online Library or from the author.

## Acknowledgements

Y.L. acknowledges the funding support provided by China Scholarship Council (CSC). The authors are thankful to N. Stepanov, S. Zherebtsov, and G. Salishchev for providing the initial alloy. The authors are also thankful to Dr. X. Sauvage for the discussion of APT results. Dr. A. Mazilkin is acknowledged for the support in discussion. This work was partly carried out with the support of the Karlsruhe Nano-Micro Facility (KNMF, www.knmf.kit.edu), a Helmholtz Research Infrastructure at Karlsruhe Institute of Technology.

Open Access funding enabled and organized by Projekt DEAL.

## Conflict of Interest

The authors declare no conflict of interest.

## Data Availability Statement

The data that support the findings of this study are available on request from the corresponding author. The data are not publicly available due to privacy or ethical restrictions.

## Keywords

atom probe tomography, grain boundary segregation, high-entropy alloys, high-pressure torsion

Received: October 11, 2022  
Revised: November 21, 2022  
Published online:

- [1] B. Cantor, I. T. H. Chang, P. Knight, A. J. B. Vincent, *Mater. Sci. Eng. A* **2004**, 375–377, 213.
- [2] G. Laplanche, A. Kostka, O. M. Horst, G. Eggeler, E. P. George, *Acta Mater.* **2016**, 118, 152.
- [3] F. Otto, N. L. Hanold, E. P. George, *Intermetallics* **2014**, 54, 39.
- [4] Z. Han, W. Ren, J. Yang, Y. Du, R. Wei, C. Zhang, Y. Chen, G. Zhang, *J. Alloys Compd.* **2019**, 791, 962.
- [5] F. Otto, A. Dlouhý, C. Somsen, H. Bei, G. Eggeler, E. P. George, *Acta Mater.* **2013**, 61, 5743.
- [6] Z. Wu, C. M. Parish, H. Bei, *J. Alloys Compd.* **2015**, 647, 815.
- [7] M. V. Klimova, A. O. Semenyuk, D. G. Shaysultanov, G. A. Salishchev, S. V. Zherebtsov, N. D. Stepanov, *J. Alloys Compd.* **2019**, 811, 152000.
- [8] Z. Li, *Acta Mater.* **2019**, 164, 400.
- [9] A. P. Zhilyaev, T. G. Langdon, *Prog. Mater. Sci.* **2008**, 53, 893.
- [10] R. Z. Valiev, R. K. Islamgaliev, I. V. Alexandrov, *Prog. Mater. Sci.* **2000**, 45, 103.
- [11] Y. Lu, A. Mazilkin, T. Boll, N. Stepanov, S. Zherebtsov, G. Salishchev, É. Ódor, T. Ungar, E. Lavernia, H. Hahn, Y. Ivanisenko, *Materialia* **2021**, 16, 101059.
- [12] G. B. Rathmayr, R. Pippin, *Acta Mater.* **2011**, 59, 7228.
- [13] X. Sauvage, Y. Ivanisenko, *J. Mater. Sci.* **2007**, 42, 1615.
- [14] Y. Ivanisenko, X. Sauvage, A. Mazilkin, A. Kilmametov, J. A. Beach, B. B. Straumal, *Adv. Eng. Mater.* **2018**, 20, 1800443.
- [15] A. Heczal, M. Kawasaki, J. L. Lábár, J. Il Jang, T. G. Langdon, J. Gubicza, *J. Alloys Compd.* **2017**, 711, 143.
- [16] B. Schuh, F. Mendez-Martin, B. Völker, E. P. George, H. Clemens, R. Pippin, A. Hohenwarter, *Acta Mater.* **2015**, 96, 258.
- [17] H. Shahmir, J. He, Z. Lu, M. Kawasaki, T. G. Langdon, *Mater. Sci. Eng. A* **2016**, 676, 294.
- [18] W. Skrotzki, A. Pukenas, E. Odor, B. Joni, T. Ungar, B. Völker, A. Hohenwarter, R. Pippin, E. P. George, *Crystals* **2020**, 10, 336.
- [19] A. V. Podolskiy, Y. O. Shapovalov, E. D. Tabachnikova, A. S. Tortika, M. A. Tikhonovsky, B. Joni, E. Ódor, T. Ungar, S. Maier, C. Rentenberger, M. J. Zehetbauer, E. Schafner, *Adv. Eng. Mater.* **2020**, 22, 1900752.
- [20] A. Semenyuk, M. Klimova, D. Shaysultanov, G. Salishchev, S. Zherebtsov, N. Stepanov, *J. Alloys Compd.* **2021**, 888, 161452.
- [21] T. Müller, M. W. Kapp, A. Bachmaier, P. Felfer, R. Pippin, *Acta Mater.* **2019**, 166, 168.
- [22] A. Pichler, E. Arzt, *Acta Metall. Mater.* **1994**, 42, 3785.
- [23] G. R. Love, *Acta Metall.* **1964**, 12, 731.
- [24] Y. Amouyal, S. V. Divinski, L. Klingner, E. Rabkin, *Acta Mater.* **2008**, 56, 5500.
- [25] D. Setman, E. Schafner, E. Korznikova, M. J. Zehetbauer, *Mater. Sci. Eng. A* **2008**, 493, 116.
- [26] K. Lu, C. F. Huo, Y. He, J. Yin, J. Liu, Q. Peng, W. P. Guo, Y. Yang, Y. W. Li, X. D. Wen, *J. Phys. Chem. C* **2018**, 122, 23191.
- [27] I. V. Kireeva, Y. I. Chumlyakov, A. V. Vyrodova, Z. V. Pobedennaya, I. Karaman, *Mater. Sci. Eng. A* **2020**, 784, 139315.
- [28] N. Stepanov, M. Tikhonovsky, N. Yurchenko, D. Zyabkin, M. Klimova, S. Zherebtsov, A. Efimov, G. Salishchev, *Intermetallics* **2015**, 59, 8.
- [29] W. Abuzaid, H. Sehitoglu, *Mater. Charact.* **2017**, 129, 288.
- [30] Q. Ding, H. Bei, X. Wei, Y. Gao, Z. Zhang, *Mater. Today Nano* **2021**, 14, 100110.
- [31] S. Huang, W. Li, S. Lu, F. Tian, J. Shen, E. Holmström, L. Vitos, *Scr. Mater.* **2015**, 108, 44.